Supporting Information for

Atomic-Scale Characterization of Commensurate and Incommensurate Vacancy Superstructures in Natural Pyrrhotites

Lei Jin,[1,a)] Dimitrios Koulialias,[2,3] Michael Schnedler,[4] Andreas U. Gehring,[2] Mihály Pósfai,[5] Philipp Ebert,[4] Michalis Charilaou,[6] Robin E. Schäublin,[3] Chun-Lin Jia,[1] Jörg F. Löffler,[3] and Rafal E. Dunin-Borkowski,[1,3,4]

[1]Ernst Ruska-Centre for Microscopy and Spectroscopy with Electrons, Forschungszentrum Jülich GmbH, 52425 Jülich, Germany

[2]Institute of Geophysics, ETH Zurich, 8093 Zurich, Switzerland

[3]Laboratory of Metal Physics and Technology, Department of Materials, ETH Zurich, 8093 Zurich, Switzerland

[4]Institute for Microstructure Research, Peter Grünberg Institute, Forschungszentrum Jülich GmbH, 52425 Jülich, Germany

[5]Department of Earth and Environmental Sciences, University of Pannonia, H8200 Veszprém, Hungary

[6]Department of Physics, University of Louisiana at Lafayette, Lafayette LA 70504, USA

a) *E*-mail: l.jin@fz-juelich.de

Procedure used to determine the angular difference between 60º- or 180º-rotated 4C pyrrhotite twins in Figure 3 and different twin variants and superstructures in Figure 4 in the main text

Step 1. Starting from a sequence of diffraction images, the central diffraction spot is cut out from each one and used to determine the relative displacements between them (left panel). On this basis, spatial drift correction is applied to the dataset, in order to obtain a set of aligned diffraction images (right panel), as described by Schaffer et al. (2004).

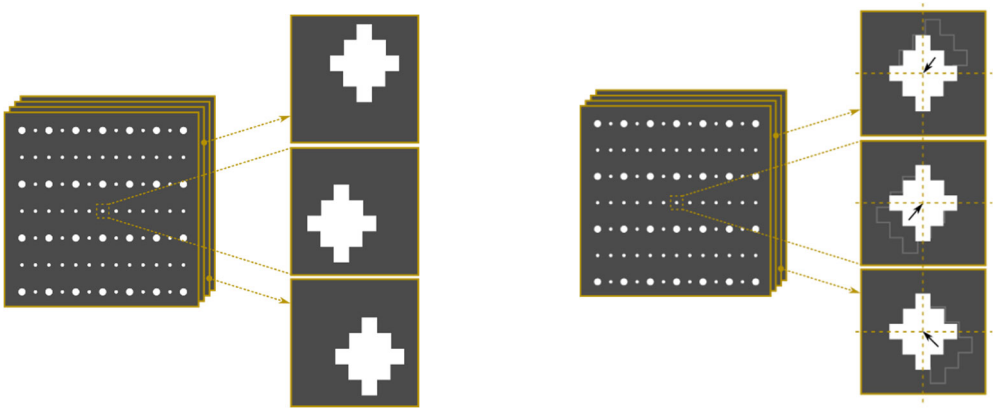

Raw dataset Aligned dataset

Step 2. In order to minimize the influence of intensity fluctuations between the diffraction spots on principal component analysis, an area in the center of each diffraction pattern that had rather homogeneous spot intensities was selected. The diffraction spot intensities in this region were then equalized by: (i) applying an offset correction; (ii) taking the square root of the resulting image; (iii) cutting off intensities exceeding an upper limit.

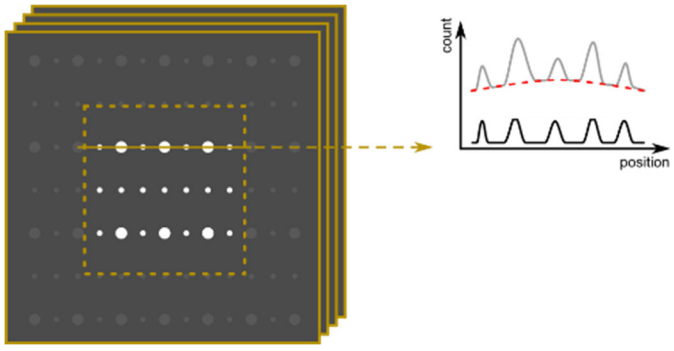

Step 3. The equalized images are improved by selecting a smaller and more homogeneous area and applying further spatial drift correction. In this step, all of the spots in the selection were used.

Step 4. The final processed diffraction images were used as input for non-negative matrix factorization/decomposition using Hyperspy software (de la Peña et al. 2011).

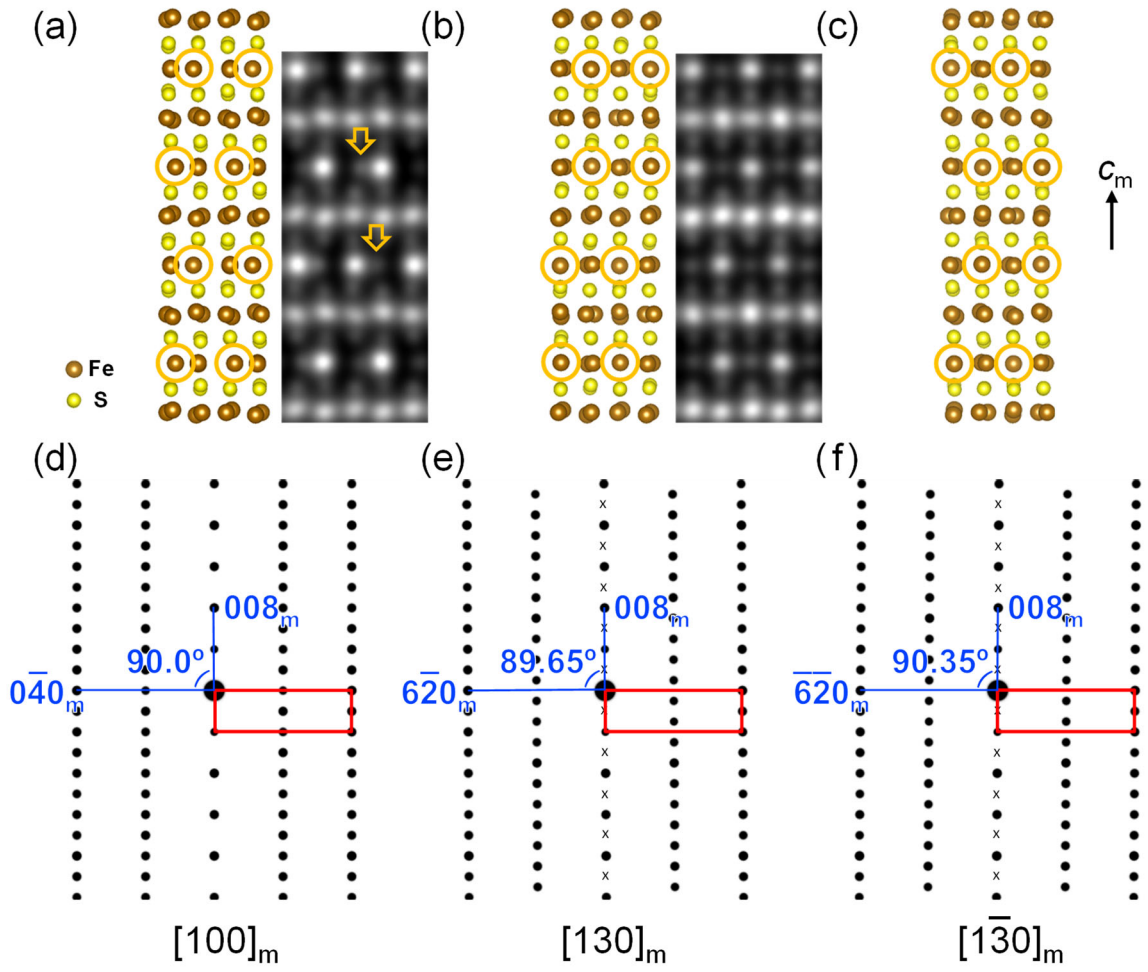

Figure S1 (a-c) Atomic projections and corresponding simulated HAADF STEM images along (a) $[100]_m$, (b) $[130]_m$ and (c) $[1\bar{3}0]_m$ (*i.e.*, hexagonal <$1\bar{1}00$>-type axes). The simulations were performed for a sample thickness of 10.7 nm. The atomic columns that contain Fe vacancies are marked by orange circles. Atomic column shifts in (a) are indicated by arrows. (d-f) Simulated electron diffraction patterns along (d) $[100]_m$, (e) $[130]_m$ and (f) $[1\bar{3}0]_m$, calculated on the basis of kinematical electron diffraction theory. The primary NiAs-type reciprocal lattice is marked by red rectangles.

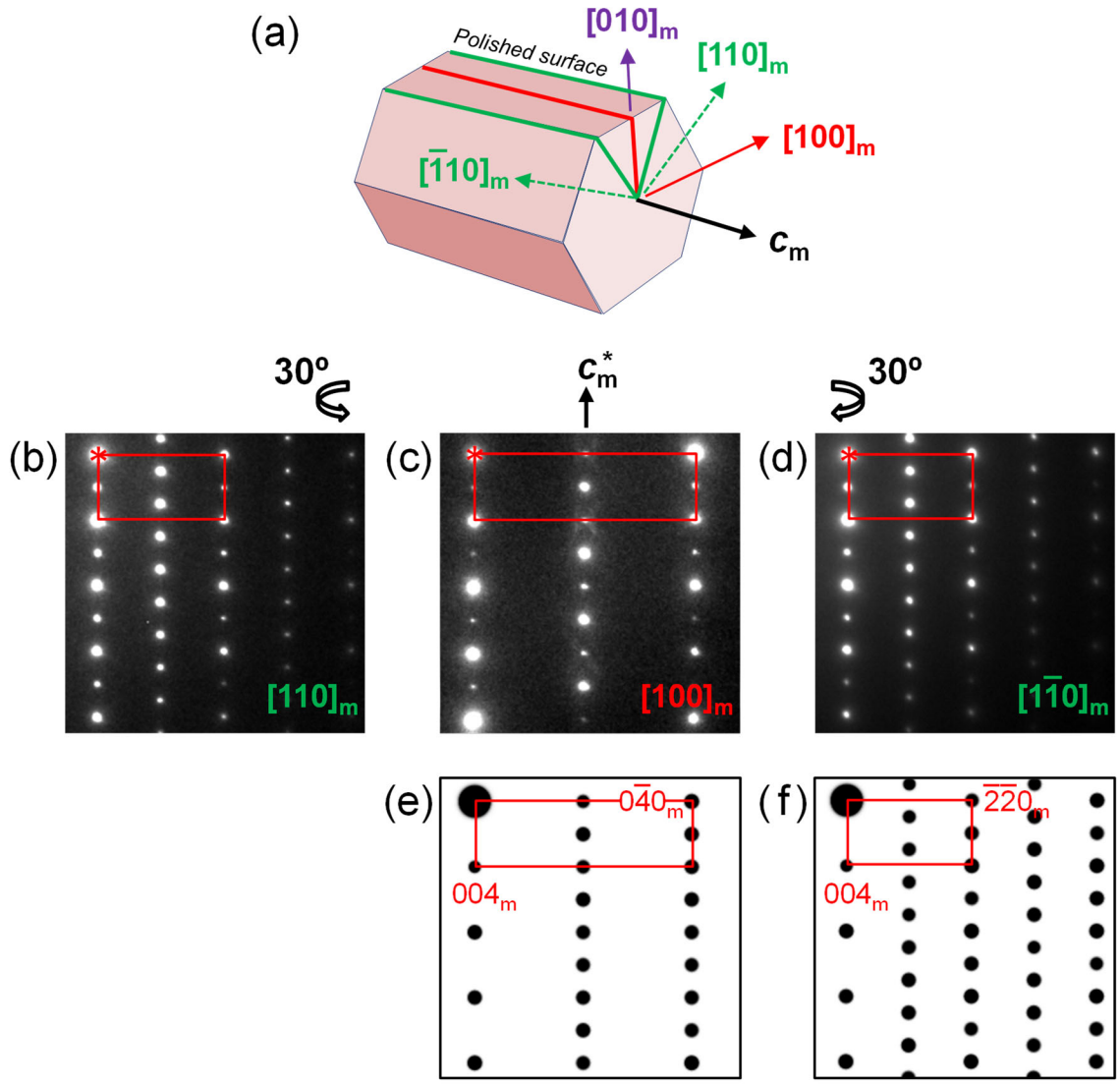

Figure S2 (a) Schematic diagram of the geometry of a natural pyrrhotite sample collected from the Auerbach region in Hesse, Germany. (b-d) Selected area electron diffraction patterns recorded from a cross-sectional lamella (marked in red in (a)) along (b) $[110]_m$, (c) $[100]_m$ and (d) $[1\bar{1}0]_m$, respectively. (e,f) Simulated electron diffraction patterns viewed along $[100]_m$ and $[110]_m$-type directions, calculated on the basis of kinematical electron diffraction theory.

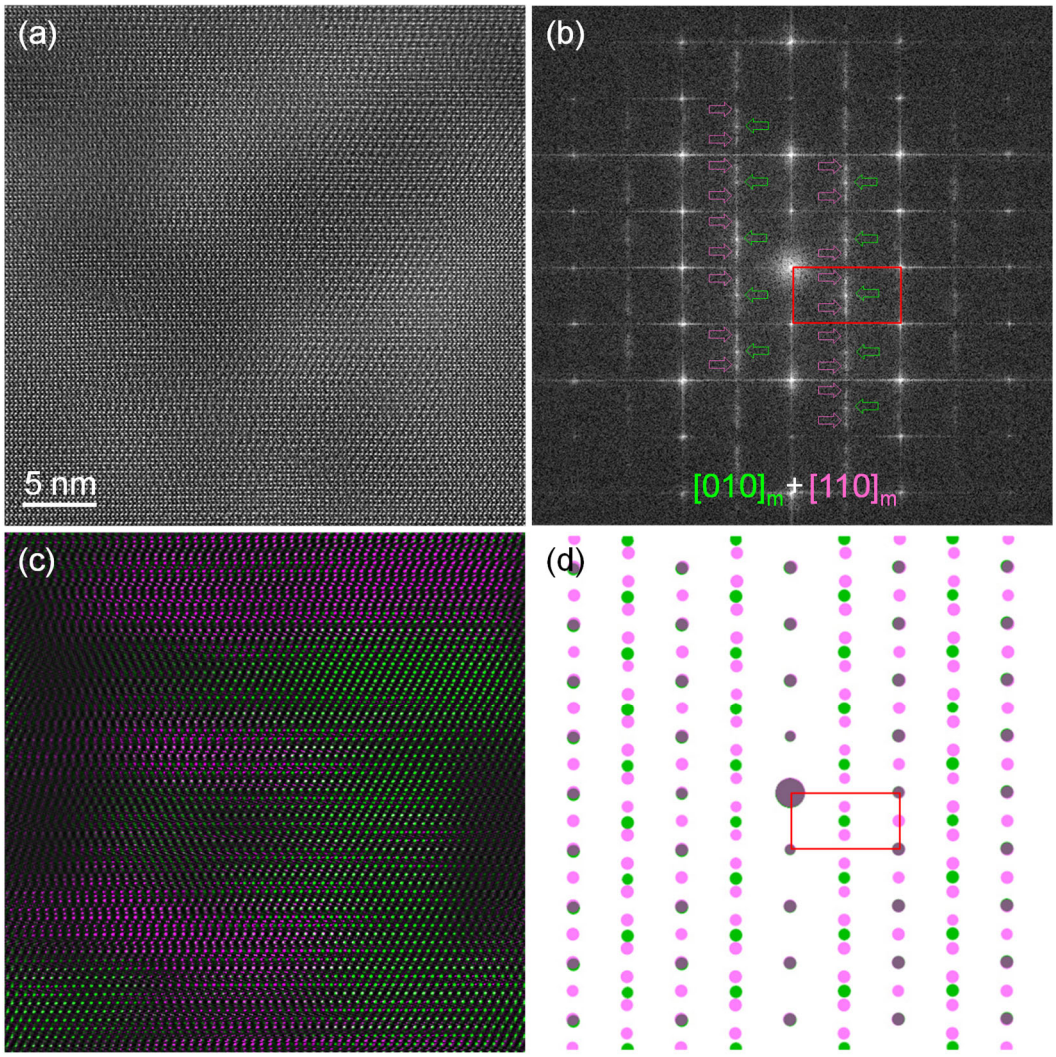

Figure S3 (a) Noise-filtered HAADF STEM image of a nanoscale intergrowth of 4C $[110]_m$-type and $[010]_m$ twin variants. (b) Fast Fourier transform (FFT) of (a). (c) Color-coded composite inverse Fourier transform (IFT) image. The green color marks the $[010]_m$ variant, while the magenta color marks the $[110]_m$-type variant. Each component IFT image was obtained using spots marked by green and magenta arrows in (b). (d) Composite electron diffraction pattern, which was obtained by combining $[010]_m$ (green) and $[110]_m$-type (magenta) contributions and is in close agreement with the FFT pattern shown in (b). The pattern was calculated on the basis of kinematical electron diffraction theory. The red rectangles in (b) and (d) mark the primary NiAs-type reciprocal lattice.

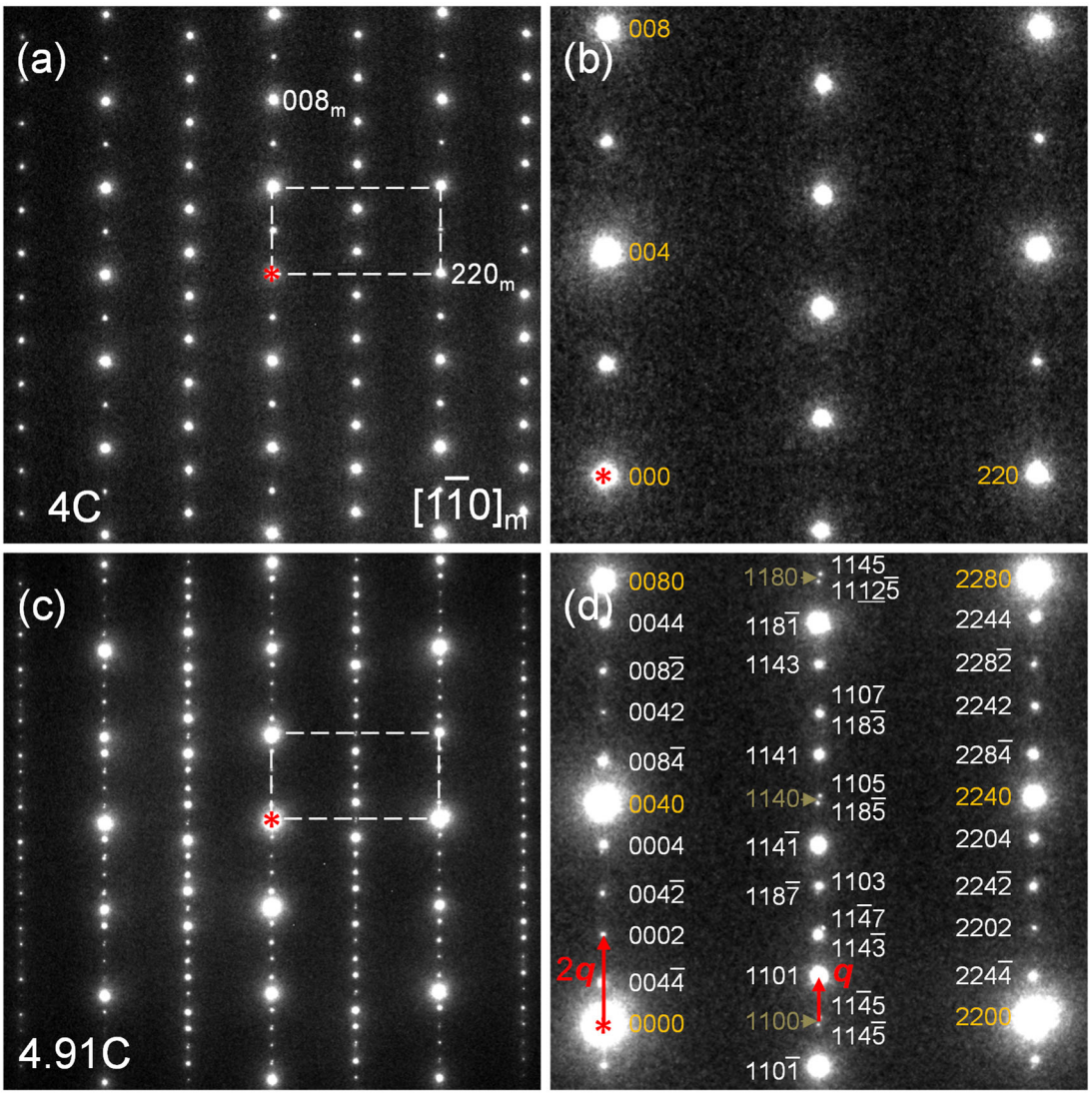

Figure S4 Selected area electron diffraction patterns recorded from (a) the 4C pyrrhotite matrix and (c) the incommensurate superstructure. The areas of the sample from which the electron diffraction patterns were recorded are each approximately 200 nm in diameter. (b,d) show magnified regions of (a,c) and have indices overlaid. The subscript "m" has been omitted for clarity. The incommensurate structure is indexed on the basis of the notation used for 4C pyrrhotite. The 4.91C structure was identified based on the relation $|\boldsymbol{g}_{0040}| / |\boldsymbol{q}| = 4.91$. Details of the indexing are described by Harries et al. (2011). The rectangles show the primary NiAs-type reciprocal lattice.

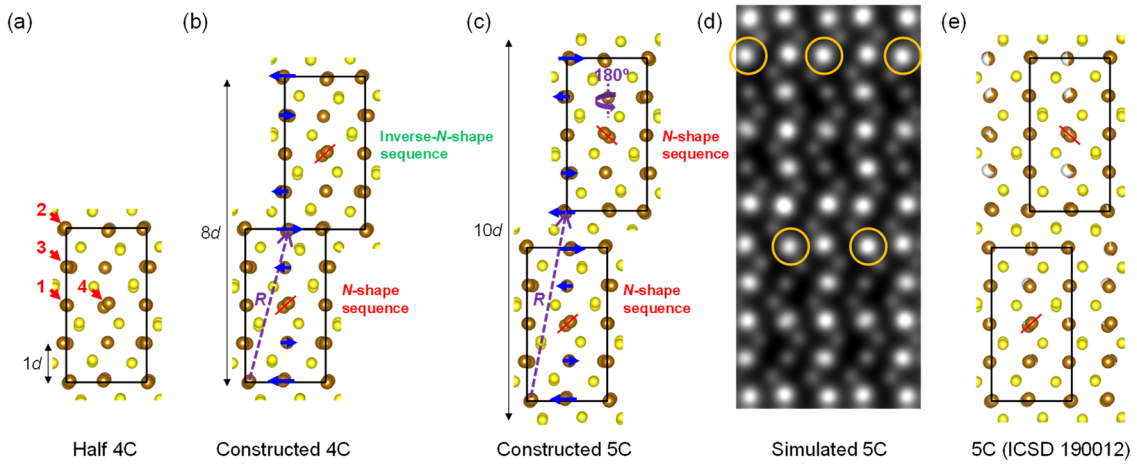

Figure S5 Construction of supercells of pyrrhotite and corresponding simulations. (a) $[110]_m$-type projection of half of the minimal asymmetric unit of 4C pyrrhotite taken from the model proposed by Tokonami et al. (1972) (ICSD 42491). (b) The full 4C pyrrhotite model can be created by copying the unit shown in (a) and shifting it with a displacement of $\boldsymbol{R} = \sim 1/8\ [\bar{1}\ 30]_m + 1/2\ [001]_m = 1.177$ nm. An additional shift of $\sim 1/8\ [110]_m = 0.172$ nm is required in the viewing direction to match the S sublattice. The shift vectors (denoted by blue arrows) correspond to an *N*-shaped sequence in the lower half and an inverse-*N*-shaped sequence in the upper half. (c) A 5C pyrrhotite supercell can be constructed by copying, performing a 180º twinning operation and then shifting the unit in (a) with a displacement of $\boldsymbol{R} = \sim 1/8\ [\bar{1}30]_m + 5/8\ [001]_m = 1.455$ nm, as shown in (c). No extra shift in the viewing direction is needed. This operation leads to two *N*-shaped sequences, with an additional 1*d* section between them. The resulting supercell has the formula Fe_9S_{10} (*i.e.*, ideal 5C). (d) Simulated HAADF STEM image created using the supercell shown in (c). Compared to the experimental images shown in Figures 11b,c in the main text, the sites that are marked by orange circles have higher intensity, resulting in the need for further modifications. (e) Projection of the 5C model (ICSD 190012; Liles and de Villiers 2012) along the equivalent axis to (a), showing very close atomic features, *i.e.*, atomic column shifts and splitting, to those shown in (c), suggesting that the constructed 5C model is practically reasonable.

References:

Schaffer, B., Grogger, W., and Kothleitner, G. (2004) Automated spatial drift correction for EFTEM image series. Ultramicroscopy, 102, 27-36.

de la Peña, F., Ostasevicius, T., Fauske, V. T., Burdet, P., Jokubauskas, P., Nord, M., Prestat, E., Sarahan, M., MacArthur, K.E., Johnstone, D.N., Taillon, J., Caron, J., Furnival, T., Eljarrat, A., Mazzucco, S., Migunov, V., Aarholt, T., Walls, M., Winkler, F., Martineau, B., Donval, G., Hoglund, E.R., Alxneit, I., Hjorth, I., Zagonel, L.F., Garmannslund, A., Gohlke, C., Iyengar, I., and Chang, H.-W. (2011) Hyperspy software package, http://dx.doi.org/10.5281/zenodo.583693

Harries, D., Pollok, K., and Langenhorst, F. (2011) Translation interface modulation in NC-pyrrhotites: Direct imaging by TEM and a model toward understanding partially disordered structural states. American Mineralogist, 96, 716-731.

Liles, D.C., and de Villiers, J.P.R. (2012) Redetermination of the structure of 5C pyrrhotite at low temperature and at room temperature. American Mineralogist, 97, 257-261.

Tokonami, M., Nishiguchi, K., and Morimoto, N. (1972) Crystal structure of a monoclinic pyrrhotite (Fe_7S_8). American Mineralogist, 57, 1066-1080.